PAPER

Robust lanthanide emitters in polyelectrolyte thin films for photonic applications

IOP Publishing Nanotechnology
Nanotechnology 29 (2018) 075302 (9pp) https://doi.org/10.1088/1361-6528/aaa325

Robust lanthanide emitters in polyelectrolyte thin films for photonic applications

Andrew S Greenspon[1,3], Brandt L Marceaux[2] and Evelyn L Hu[1,3]

[1] John A Paulson School of Engineering and Applied Sciences, Harvard University, Cambridge, Massachusetts 02138, United States of America
[2] Department of Science, Technology and Mathematics, Gallaudet University, Washington DC 20002, United States of America

E-mail: agreenspon@g.harvard.edu and ehu@seas.harvard.edu

Received 3 November 2017, revised 11 December 2017
Accepted for publication 20 December 2017
Published 15 January 2018

Abstract

Trivalent lanthanides provide stable emission sources at wavelengths spanning the ultraviolet through the near infrared with uses in telecommunications, lighting, and biological sensing and imaging. We describe a method for incorporating an organometallic lanthanide complex within polyelectrolyte multilayers, producing uniform, optically active thin films on a variety of substrates. These films demonstrate excellent emission with narrow linewidths, stable over a period of months, even when bound to metal substrates. Utilizing different lanthanides such as europium and terbium, we are able to easily tune the resulting wavelength of emission of the thin film. These results demonstrate the suitability of this platform as a thin film emitter source for a variety of photonic applications such as waveguides, optical cavities, and sensors.

Supplementary material for this article is available online

Keywords: lanthanides, luminescence, polyelectrolytes, surface chemistry, self-assembly

(Some figures may appear in colour only in the online journal)

1. Introduction

Methods for controlling the position, density, and overall number of emitters on surfaces can lead to stronger, more controllable light–matter interactions on patterned surfaces and in integrated nanostructures such as waveguides and optical cavities. The choice of the emitter, as well as its placement, is critical for photonic applications. Desirable emitters satisfy the wavelength of interest for an application, readily integrate with a cavity or other photonic structure, and demonstrate high optical efficiency and long-term robustness. Optimal interaction with a cavity requires both spatial and spectral alignment of the emitter with the electric field modes of an optical cavity [1]. For plasmonic enhancement, the distance of an emitter from a metal surface can significantly affect the emission of a molecule due to changes in its electric and magnetic dipole transitions [2]. In addition, careful placement of the emitter with respect to the metal substantially influences the degree of quenching of optical emission. Thus, it is highly desirable to be able to form easily-deposited, uniform thin (~10–20 nm) films of optically active material that will not quench in the presence of metal substrates.

The trivalent lanthanides (Ln^{3+}) are emitters that offer a wealth of possibilities as efficient optical sources. They amplify and transfer signals in telecommunications [3], form the basis of phosphors for lighting [4], and act as luminescent bio-probes due to their long fluorescence lifetimes [5]. Lanthanides can be embedded in fluids and gels with tunable emission by varying temperature, solution pH, mechanical stimuli, and chemical reactions [6, 7]. They have also been incorporated into inks for anti-counterfeiting measures [8]. In addition, lanthanides have been doped into crystalline phosphors for upconversion from near-infrared to blue [9], green [10], and white [11] color emission for lighting or flat panel devices. The temperature-dependent emission of such crystals can also be used to develop optical temperature sensors. Lanthanide-doped nanoparticles can also be functionalized with amine groups to increase water solubility and improve

[3] Authors to whom any correspondence should be addressed.

uptake by biological organisms for imaging [12, 13]. Such amine-functionalized nanoparticles have been shown to have low toxicity for cells.

This paper describes the application of lanthanide emitters, incorporated within polyelectrolyte multilayers (PEMs): the PEMs provide a well-controlled means of introducing a uniform layer of lanthanide emitters onto a surface. We utilize lanthanides in a chelated form, bound to three dipicolinate (DPA) molecules to form the organometallic complex lanthanide(III) tris(dipicolinate) ($Ln(DPA)_3^{3-}$) or simply Ln-DPA. In this form, lanthanides such as europium (Eu) or terbium (Tb) demonstrate distinctive narrow emission lines, long lifetimes, relatively high quantum yields, and insensitivity to photobleaching [5]. In addition, the DPA more readily absorbs ultraviolet light compared to the lanthanide and transfers this energy to the lanthanide for radiative emission, increasing the overall optical efficiency [14]. In addition, the Ln-DPA complexes are water soluble and compatible with the layering process described herein [8].

We bind two different lanthanides in varying ratios to PEM films to demonstrate their high quality optical emission and the ability to color-tune the thin film emission. The lanthanide emission is robust and long-lived; the emission intensity does not decay over a period of months after preparation of the samples. Even more striking, the lanthanide emission is not quenched even when the Ln-DPA is brought into close proximity with a metallic gold surface and may in fact be enhanced. We have also observed a correlation between total luminescence intensity and number of layers in a PEM, suggesting that we have some control over the amount of lanthanide bound to a PEM and that the lanthanide complex diffuses below the surface of the PEM towards the substrate. These results show that this system exhibits versatility and stability for integration into a wide variety of nanostructures or devices.

2. Methods

2.1. Overview of thin film preparation

PEMs were prepared on silicon (100) wafers, ground and polished quartz microscope slides (Chemglass Life Sciences number CGQ-0640), and e-beam deposited gold films on quartz slides. The multilayers comprised a 'strong' polyelectrolyte poly (4-styrene sulfonate) (PSS) and a 'weak' polyelectrolyte poly (allylamine hydrochloride) (PAH). This combination of polyelectrolytes has been previously utilized, and the approach described: the 4-styrenesulfonate side chains of the PSS are all negatively charged regardless of solution pH, whereas the percentage of charged amine side chains in PAH depends on the pH of solution [15]. Beginning with a single layer of PAH, we then layer oppositely charged PSS and PAH to a desired thickness of PEM. We refer to a layer of positively followed by negatively charged polyelectrolyte as a single bilayer. Thin film absorption measurements were carried out in an Agilent Cary 60 UV–vis spectrophotometer. Increased absorption with number of bilayers confirmed the effectiveness of the layering process (figure S1(a) supporting information is available online at stacks.iop.org/NANO/29/075302/mmedia).

To incorporate the lanthanide emitters, the prepared PEM samples were dipped into pre-made Eu- or Tb-DPA solutions. As the Ln-DPA complex has a net negative charge, we expected that it should selectively attach to a multilayer structure where positively charged PAH is the uppermost layer; concomitantly, we expected little or no binding to a PEM with negatively charged PSS as the top layer.

When multilayers were prepared on quartz substrates having 2, 4, 6, and 8 bilayers, with an additional, upperqmost layer of positively charged PAH, subsequent dipping into a solution of Ln-DPA resulted in the binding or incorporation of the Ln-DPA onto the PEM. This was confirmed through UV–vis absorption spectroscopy, which revealed increased absorption due to DPA, which has characteristic absorption peaks centered at 280 and 272 nm in addition to broad absorption below 240 nm (figures S1(b) and (c), supporting information). The presence of the lanthanide was further confirmed through micro-photoluminescence (μPL) measurements.

However, when multilayers of different thicknesses were prepared with PSS as the uppermost layer, subsequent dipping into a Eu-DPA solution produced no signature of Eu-DPA either through UV–vis absorption measurement or μPL scans on the sample. The charge-selective attachment of the lanthanide containing layer offers a means of laterally patterning regions of lanthanide emitters. For example, previous work with this polyelectrolyte system has shown the ability to create macroscopic domains by selectively exposing some PEM regions to low pH water droplets that increase the positive charge of the PAH in order to selectively bind a negatively charged dye [16].

The full process is indicated schematically in figure 1. The schematic highlights the incorporation of a generic Ln-DPA where the central ion can be almost any lanthanide but is either Eu or Tb in our experiments. The chemistry will be the same for any lanthanide bound in this configuration. We last note that while the Ln-DPA rests on the surface of the structure in the schematic, experiments described herein suggest that the molecule in fact diffuses into the PEM structure to some degree.

2.2. Preparation of polyelectrolyte and rinse solutions

Polyelectrolyte solutions for layering were prepared with 18.2 mega-ohm de-ionized (DI) water from a Millipore Milli-Q system. PAH of molar weight 58 000 was used as a weak positive polyelectrolyte and PSS of molar weight 70 000 was used as a strong negative polyelectrolyte, both from Sigma Aldrich. The polyelectrolytes were dissolved in water to form 10 mM PAH and PSS solutions (93.554 and 207.194 g mol^{-1} per repeat unit respectively). The 10 mM PAH solution was adjusted to pH 9.3 using NaOH solutions. In addition, three rinse solutions of DI water were prepared for each

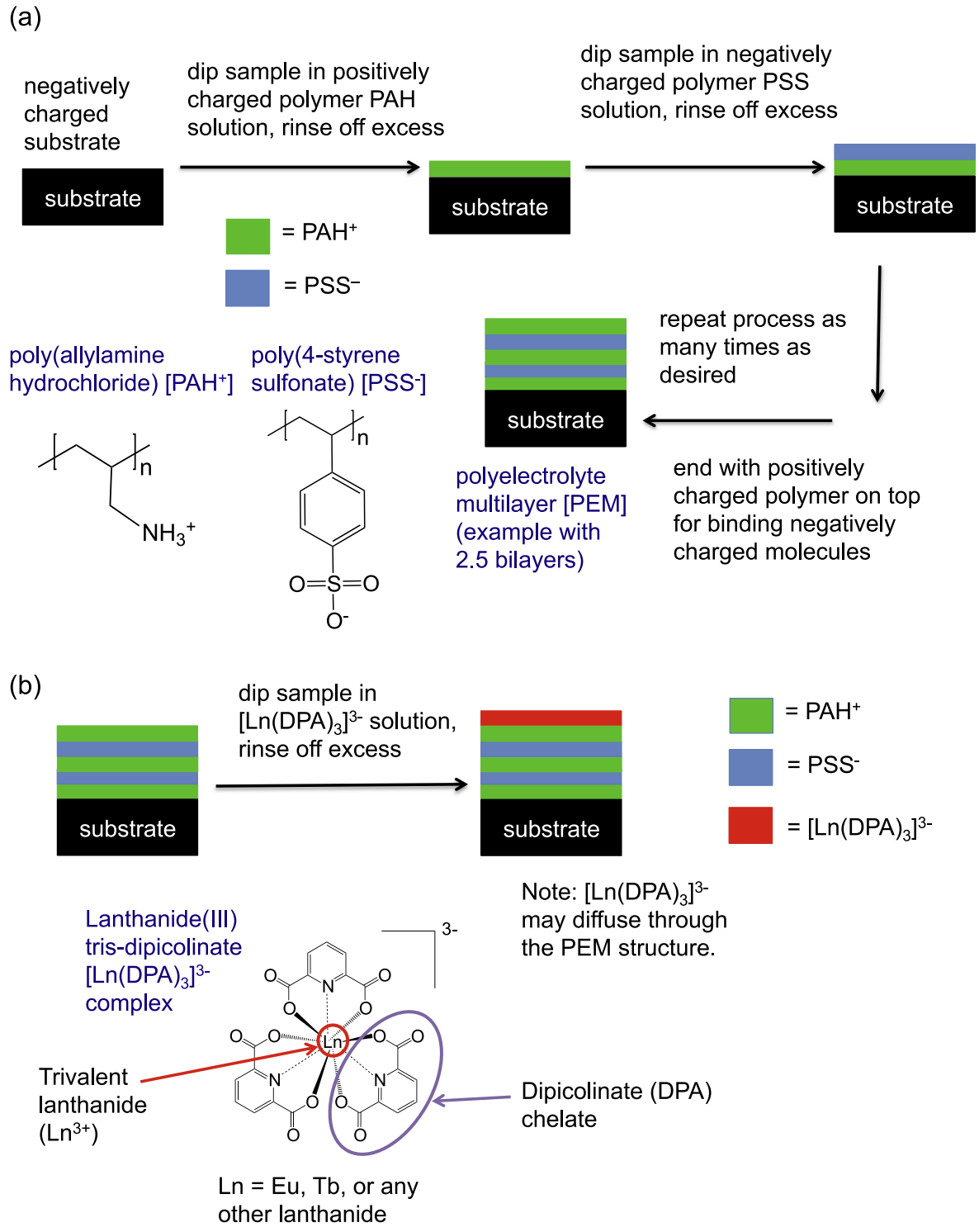

Figure 1. Schematic diagram of layering procedures. (a) Process for layer-by-layer electrostatic deposition of PAH and PSS to form a PEM. (b) Process of binding and incorporating Ln-DPA molecules into the PEM, where Ln can be almost any lanthanide.

polyelectrolyte solution. NaCl was added to all solutions at a concentration of 20 mM.

2.3. Preparation of quartz and silicon substrates, and layering process

Immediately prior to layering, substrates were cleaned by sonication in acetone and isopropanol and dried with compressed air. Samples were then placed in a Piranha etch mixture (3:1 of 95%–98% sulfuric acid: 30% hydrogen peroxide) for at least 10 min to clean the substrate surface and ensure a negatively charged surface. Samples were then placed in DI water and dried with compressed air. One end of each sample was then attached to a clip to allow dipping into the desired solutions. Prior to dipping, the PAH solution was adjusted to pH 9.3 with 0.5 M NaOH. Every other solution

was not pH adjusted. Samples were initially dipped in the positive 10 mM PAH followed by 10 mM PSS until completing the desired number of layers. For each polyelectrolyte solution, samples were dipped for six minutes, followed by dips in three rinse solutions at two minutes, one minute, and one minute respectively. After the last polyelectrolyte layering, samples were placed under a DI water stream for 30–60 s to fully remove any excess polyelectrolytes. Samples were then dried with compressed air. Samples were placed in vacuum and protected from light with aluminum foil when not being characterized.

2.4. Preparation of Eu- and Tb-DPA crystals

Dipicolinic acid (2.0 g, molar weight 167.12 g mol^{-1}, Sigma Aldrich) was dissolved in 60 ml DI water, and the solution was brought to a boil. $EuCl_3 \cdot 6H_2O$ (1.462 g, molar weight 366.41 g mol^{-1}, Sigma Aldrich) was added to this solution. The solution was allowed to cool and 2 M NaOH followed by 0.1 M NaOH were added dropwise until the solution reached a pH of 8.0. Addition of NaOH too rapidly will lead to the irreversible formation of a white precipitate of europium oxide or hydroxide. The solution was left in a fume hood to crystalize. Eu-DPA crystals were removed, powdered with mortar and pestle and stored in a vacuum box. We estimate a molar mass of 800 g for $Eu(DPA)_3{}^{3-}$ crystals in order to take into account Na^+ and water molecules contained in the crystals. Tb-DPA crystals were prepared in a similar manner using $TbCl_3 \cdot 6H_2O$ (molar weight 373.38 g mol^{-1}, Alfa Aesar).

2.5. Embedding Ln-DPA molecules in PEMs

A 10 mM Eu-DPA solution was prepared by dissolving 0.496 g in 62 ml DI water. The pH was then adjusted to pH 4.0 with 1 M HCl. Prepared PEM samples were dipped in this solution for 10 min. Afterward, samples were placed under a DI water stream for 30–60 s to fully remove any excess Eu-DPA. Samples were then dried with compressed air. Samples were placed in vacuum and protected from light with aluminum foil when not being characterized.

10 mM total Eu- and Tb-DPA solutions were prepared by dissolving mixtures of Eu- and Tb-DPA in molar ratios of 15:85, 30:70, 50:50, 70:30, 85:15. The pH of each was then adjusted to pH 4.0 with 0.1 M HCl. Each prepared PEM sample was dipped in one of these solutions for 10 min. Afterward, samples were placed under a DI water stream for 30–60 s to fully remove any excess Ln-DPA. Samples were then dried with compressed air. Samples were placed in vacuum and protected from light with aluminum foil when not being characterized.

3. Results and discussions

3.1. Thickness of the PEMs

We analyzed Ln-DPA-PEMs varying in PEM thickness from 2.5 to 8.5 bilayers. UV–vis absorption measurements give us assurance of the systematic and reproducible increase in PEM thickness with increased bilayer incorporation (figure S1(a), supporting information), but cannot provide an exact value of the total thickness. To provide a general cross-calibration of PEM thickness, we formed a 11.5 bilayer PAH and PSS sample on (100) silicon substrate with PAH as the topmost layer. Eu-DPA was embedded into the sample as described above. We then used a focused ion beam to lift out a lamella from this sample containing a cross section of the PEM. The lamella was imaged with a JEOL 2100 TEM at low voltage 80 kV to minimize damage to the sample due to electron bombardment (figure S2, supporting information). Bright field TEM images of the sample allowed us to determine the thickness of this PEM to be ∼43 nm with variation in thickness of only a couple nanometers. This corresponds to an average bilayer thickness of 3.74 nm although the PSS layer is expected to be thicker than the PAH layer because the polymer side groups are much larger. (*See supporting information for further details*.) The details of each layering process, such as the substrate charge and the pH of each solution, may change the values of thickness slightly, but we believe that this calibrated assumption of 3.74 nm per bilayer thickness is a useful one to employ for our analysis.

3.2. Ln-DPA-PEM emission characteristics

The spectral characteristics and uniformity of the Ln-containing PEMs was carried out using μPL spectroscopy. For the Eu-DPA-PEMs, a LabRam Evolution Horiba Multiline Raman Spectrometer was used, with a continuous wave 532 nm laser and a 100x objective. Samples with Tb^{3+} emitters required shorter wavelength excitation; in this case, a home-built confocal microscope set-up was used with a pulsed 380 nm laser and a 100x objective. Pure Tb-DPA and Eu-DPA crystals were also scanned with the 380 nm laser.

We first collected μPL spectra of Ln-DPA crystals to compare to those molecules embedded in PEMs. We took a drop of prepared Eu-DPA and Tb-DPA solutions and placed them on quartz substrates. We then let the solution evaporate, leaving the pure crystal on the substrate. Figure 2(a) shows the μPL spectrum of Eu^{3+} and Tb^{3+} from these crystals. Eu^{3+} has a peak emission at ∼616 nm with a full-width-half-maximum (FWHM) of ∼1.82 nm. Tb^{3+} has multiple overlapping peaks, making it difficult to measure the FWHM of individual peaks.

Figure 2(b) shows the average μPL spectrum of a Eu-DPA-PEM with 2.5 bilayers on quartz substrate, again with principal peak emission at 616 nm but a larger FWHM of ∼2.35 nm. This spectrum is an average of nine scans over a 3 × 3 grid of size on the order of millimeters across the sample. The linewidth broadening suggests the Eu^{3+} is not in as uniform an environment in the PEM as when in crystalline form, even when protected by the DPA in both cases. However, this broadened linewidth is consistent across the PEM sample.

This technique allows an easy means of tuning the emission of the Ln-DPA-PEMs by binding mixtures of Eu- and Tb-DPA to our PEMs. We began with five 2.5 bilayer PEMs layered on quartz substrates. UV–vis data shows that the absorption and therefore the thicknesses of these samples are about the same. We then made 10 mM total solutions of Eu- and Tb-DPA in varying molar ratios of Eu:Tb = 15:85,

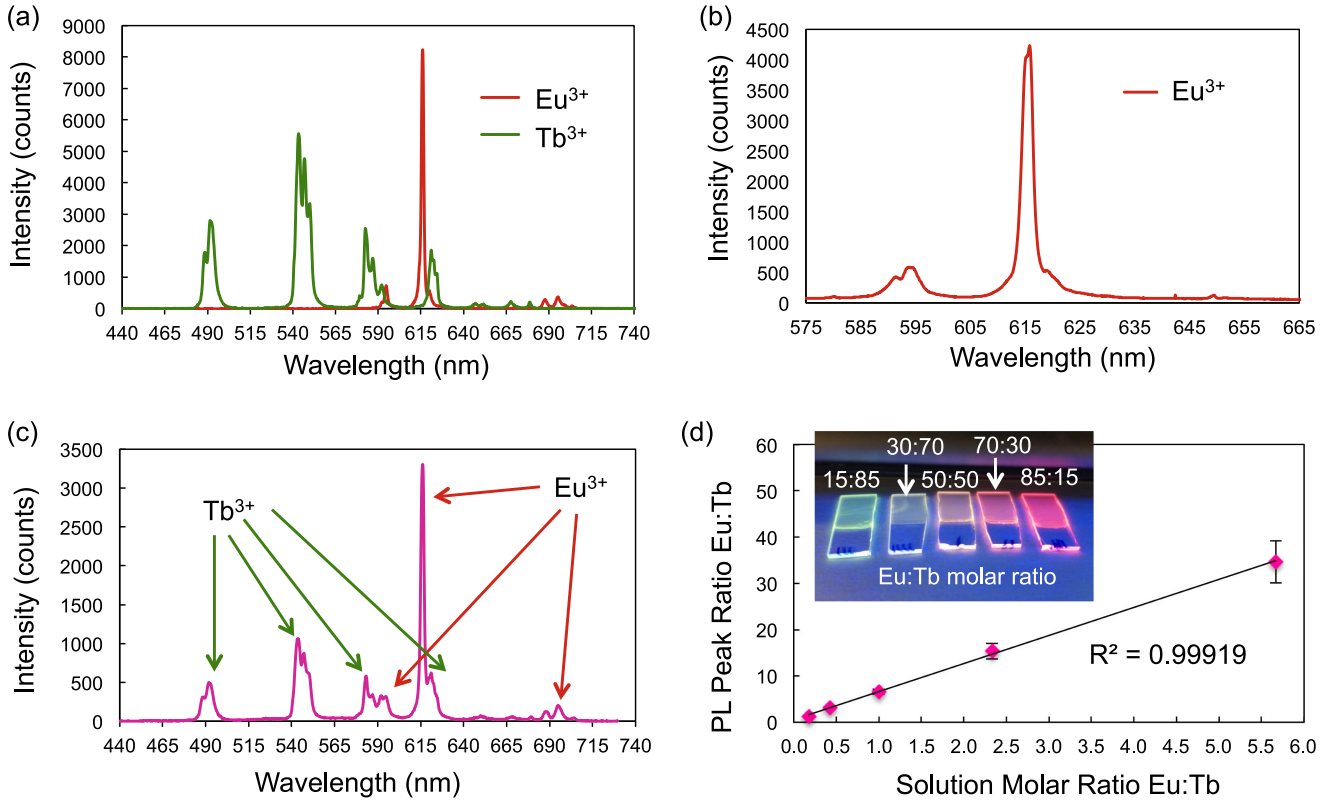

Figure 2. Emission of Eu^{3+} and Tb^{3+} bound to DPA in crystalline form and embedded in PEMs. (a) PL spectra from Eu^{3+} and Tb^{3+} emission in Eu- and Tb-DPA crystals placed on quartz substrates. Note: different amounts of 380 nm laser power were used to excite each crystal, so no comparison should be made between absolute emission intensities here. (b) Average PL from a 2.5 bilayer PEM containing Eu-DPA. (c) Average PL from a 2.5 bilayer PEM with Eu:Tb-DPA embedded at a molar ratio of 30:70. Emission peaks from Eu^{3+} and Tb^{3+} are labeled. (d) Ratio of PL emission of the largest peaks from Eu^{3+} (616.3 nm) and Tb^{3+} (543.5 nm) as compared against the molar ratio of Eu:Tb in each solution used to bind to the PEMs on quartz substrate. Inset: broad fluorescence from Eu:Tb samples when excited by a 254 nm UV lamp. The molar ratio of Eu:Tb from left to right is 15:85, 30:70, 50:50, 70:30, and 85:15.

30:70, 50:50, 70:30, and 85:15. Each PEM sample was dipped in one of these solutions and then rinsed with DI water to remove excess. UV–vis absorption spectroscopy was again used to verify the absorption of each sample was about the same, indicating that the same total amount of DPA and therefore the same total lanthanide was bound to each PEM. Samples were then scanned with μPL on a 3 $\times$ 3 grid of size on the order of millimeters, using the 380 nm pulsed laser to excite both the Eu^{3+} and the Tb^{3+} to generate light emission. Figure 2(c) shows the average multi-peak spectrum due to dipping a 2.5 bilayer PEM in a solution with Eu:Tb = 30:70 molar ratio. (see figure S3, supporting information for spectra of all samples). The FWHM of the Eu^{3+} 616 nm peak is about the same for all mixed lanthanide samples, suggesting the stability of the emission regardless of the relative ratio of different lanthanides embedded in the PEM. However, this result alone does not show that the Eu^{3+} and Tb^{3+} do not interact within the sample.

In order to compare the emission from Eu^{3+} and Tb^{3+} in each of these samples, we take the ratio of the largest peaks from each of these samples (616.3 nm for Eu^{3+}, 543.5 nm for Tb^{3+}) and compare to the molar ratio of lanthanides in the dipping solution used to bind them to the PEMs (figure 2(d)). The ratio of PL intensity between the Eu^{3+} and Tb^{3+} peaks scales linearly with the molar ratio of each lanthanide in the layering solution. This linear relation combined with the unchanged FWHM of emission peaks shows that the Eu^{3+} and Tb^{3+} emission appear to be independent of each other and controllable simply by adjusting the ratio of each component in solution. We believe there are two possible reasons for this non-interaction: (1) the low concentration of Eu and Tb means that individual Eu and Tb ions are too far from each other to have any localized interaction, and (2) the Eu and Tb are each fully encapsulated by the three DPA molecules, preventing any direct coupling to adjacent lanthanides. When the samples are excited broadly by a 254 nm UV lamp, we get bright visible fluorescence from each of these samples (figure 2(d) inset). By simply varying the ratio of these two emitters, we can controllably span the color spectrum from green to yellow, orange, and red.

Last, we note the robustness of the emitters in these mixed lanthanide samples. PL on these samples was taken days after they were prepared and three months later. The intensity of the PL peaks had not decayed noticeably (figure S4, supporting information). The image in figure 2(d) inset was taken four months after the samples were made, demonstrating the long-term preservation of the colors. Other PEM samples containing only Eu-DPA glow red when exposed to a 254 nm UV lamp many months after the samples

Table 1. Average Eu^{3+} μPL emission at different peak wavelengths in two 4.5 bilayer PEM layered samples, one on quartz and one on 100 nm Au on quartz substrate. Background signal has been subtracted to properly compare the peak intensities.

Wavelength (nm)	593.87		615.84	
	Average PL intensity (counts)	Standard deviation	Average PL intensity (counts)	Standard deviation
Eu-DPA in 4.5 bilayer PEM on quartz	705	74	5838	710
Eu-DPA in 4.5 bilayer PEM on Au	1652	468	11 375	3413

were prepared although quantitative measurements were not taken for these samples during that time period.

3.3. Comparison of Eu^{3+} emission near a dielectric and metallic surface

Our PL characterization of Ln-DPA-PEM emission on quartz revealed bright, uniform emission over substrate areas of a few square millimeters. More stringent requirements on thin film emission are imposed by metal substrates, where close proximity of the emitter to metal may result in quenching of the emission. Accordingly, we compared Eu-DPA-PEM emission from samples with PEMs bound to both quartz and gold (Au). The Au surface was made by depositing 100 nm of Au on a solvent cleaned quartz substrate using a Denton Explorer 14 E-beam Evaporator. The quartz sample was dipped in Piranha etch for 10 min followed by DI water dip and drying with compressed air to negatively charge the surface whereas the Au sample was used as-is post-deposition. Both samples were dipped in 4.5 bilayers of PAH and PSS at the same time. UV–vis absorption spectroscopy was done on the quartz sample to verify PEM binding, and x-ray photoelectron spectroscopy (XPS) with a Thermo Scientific K-Alpha+ XPS system was used to verify PEM binding to the Au sample. Using the lamella-determined value of bilayer thickness, we estimate the PEM layer on each substrate to be $\sim$16.8 nm thick.

Both samples were then dipped in Eu-DPA solution for 10 min followed by DI water rinse. μPL was then done on both samples in a 3×3 grid. The average values and experimental variation of the peak intensities at 593.87, and 615.84 nm after a background subtraction of the base level of luminescence are shown in table 1, which compares the intensities of the Eu^{3+} peak emissions for the quartz and Au substrates. Standard deviation is derived from the variation in μPL signal across the 3×3 grid. The average PL signal on the gold surface is roughly twice as large as the PL signal from the quartz surface; far from experiencing quenching of emission by the gold surface, the emission of the Eu^{3+}, situated $<$20 nm from the gold surface is robust.

XPS was used to gain more quantitative information about the composition of the Eu-DPA-PEM layer. XPS scans detect on the order of 1% Si and Au respectively for the quartz and gold substrate samples, implying that ejected substrate electrons just barely escape the sample to reach the detector. The escape depth for electrons from a material at normal incidence is defined as three times the inelastic mean free path (IMFP) or when the electron intensity has decayed to 5% of its initial value [17]. The IMFP depends on both the material the electrons are traveling through and their kinetic energy. The kinetic energy of the Au 4f and Si 2p electrons is around 1400 eV. Cumpson provides IMFP values at 1000 eV for PAH (3.9 nm) and PSS (2.9 nm) [18]. While these values are for bulk and non-mixed polyelectrolyte films as we have, we are confident that the IMFP for our films should fall within the range of 2.9–3.9 nm at 1000 eV. Using a scaling equation provided there, we find an IMFP at 1400 eV of 3.8 to 5.1 nm, leading to an approximate escape depth of 11.3–15.3 nm. The XPS data and the calculated escape depth are consistent with our earlier (TEM-based) estimate of $<$17 nm thick PEM.

XPS analysis was also used to estimate the relative amounts of Eu-DPA binding to the quartz and gold substrates. The average XPS signal strength for Eu (by atomic %) on the quartz substrate, from measurements at three different locations on the sample, was $XPS_{Eu,quartz} = 0.34 \pm 0.18$. The average signal strength on the Au substrate, from measurements at two different locations, was $XPS_{Eu,Au} = 0.65 \pm 0.10$, suggesting that the strong Eu^{3+} emission on the Au substrate may be related to a larger incorporation of Eu in the PEM. The reason for this may lie with the details of the charge state of the Au substrate and its effect on the layering process that produces the Eu-DPA-PEMs. In addition, light reflection from the Au surface may increase the PL signal collected by our objective.

We also observe that there is greater variation in the PL signal across the gold surface compared to the quartz substrate. As examined by eye, there are a number of areas of visible particulates on the Au surface as compared to the quartz surface. These particulates may have deposited on the sample from the air or from the dipping solutions, creating non-uniformities in the film. The Au surface may more readily bind such particulates compared to the quartz surface.

3.4. Variable incorporation of Eu^{3+} into the PEMs

Our initial characterization of the Ln-DPA-PEM films revealed the selective attachment of the Ln-DPA to a positively charged PAH surface, and a bright, uniform, and robust emission from the Ln-containing material. XPS analysis revealed a variation of the Eu signal for two similarly formed Eu-DPA-PEM films, depending on whether the substrate was quartz or Au. We thus further explored other possible variations in the amount of Eu^{3+} incorporated into the PEMs.

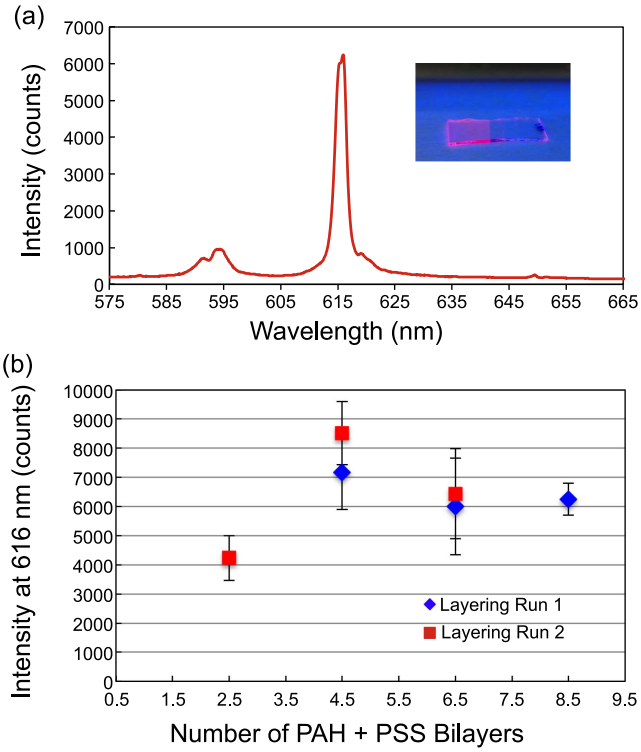

Figure 3. μPL emission of Eu^{3+} embedded in PEMs with different numbers of bilayers. (a) Average PL of Eu^{3+} embedded in 8.5 bilayers of PAH and PSS on quartz substrate. Inset: image of the sample when exposed to a 254 nm UV lamp to excite the Eu^{3+}. The region on the left was layered with polyelectrolytes whereas the region on the right was not. (b) Comparison of average PL intensity at the 616 nm Eu^{3+} peak for samples with varying numbers of bilayers, all on quartz substrate. Uncertainty bars are the standard deviation of the nine points scanned on each sample. The red square and blue diamond sets of points were layered in two separate dipping runs in order to show the reproducibility of the technique.

We formed a number of PEM samples, ranging in thickness from 2.5 to 8.5 bilayers, capped with a Eu-DPA layer, using the methods described earlier. Characterization of the Eu-DPA-PEM films was carried out through μPL spectroscopy. As before, each multilayer sample was scanned in a 3×3 grid over a 3×3 mm or 4×4 mm region depending on the size of the sample; for a given sample, there was little variation in the Eu^{3+} emission peak intensity across the sample. Figure 3(a) shows an example average μPL spectrum from an 8.5 bilayer sample. For each sample, the 616 nm peak had the same FWHM, indicating that the environment for the Eu^{3+} is similar regardless of the number of bilayers.

We observed a variation in the average PL intensity at the 616 nm peak as the number of bilayers changed (figure 3(b)). To account for small variations in the process that might characterize a particular layering run, we prepared samples in groups of three: one set comprised PEMs with 2.5, 4.5 and 6.5 bilayers, while another comprised 4.5, 6.5 and 8.5 bilayers. We therefore made two samples each with 4.5 and 6.5 bilayers in different runs to demonstrate the reproducibility of the technique. Despite the uncertainty in the values of intensity for each sample, we have confidence in the relative

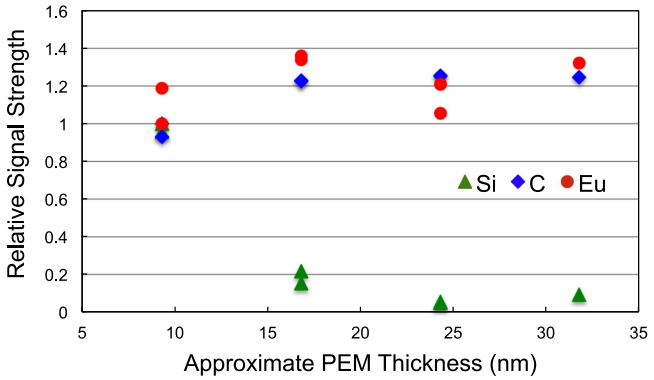

Figure 4. Relative XPS signal strength for silicon, carbon, and europium for polyelectrolyte samples of different thicknesses. Signal is normalized to one of the spot scans on the 2.5 bilayer sample.

changes in μPL intensity as we vary the number of bilayers. Across the four data points spanning 2.5–8.5 bilayers, there appears to be a rise in intensity when the PEM thickness increases from 2.5 to 4.5 bilayers, and a subsequent slight decrease as the thickness increases to 6.5 and 8.5 bilayers. It is reasonable to assume that variation in emission intensity is correlated with the amount of Eu-DPA bound to each PEM sample, and thus cross-correlative measurements using XPS are useful.

Our earlier experiments showed the strong role of surface charge in being able to bind the Eu-DPA to the PEM. If the binding and incorporation pertained to the surface alone, then for the same Eu-DPA concentration, we might assume the same amount of surface incorporation of Eu. However, the variation in PL intensity suggests that it is possible that the Eu-DPA is diffusing from the surface through the PEM during the dipping process. To gain further insight, we analyzed the XPS signal percentage of key elements as a function of PEM thickness assuming an average bilayer thickness based on the TEM lamella sample. For each layer thickness, two spots were scanned to provide an estimate of the variance in the measurement. (One of the spots for the 8.5 bilayer sample appeared irregular, so there is only one entry for that bilayer.)

In principle, XPS depth profiling should provide information on the distribution of Eu through the PEM. However, because the PEM is an organic layered structure, the sputtering rate is hard to determine, as is the precise thickness. In addition, the sputtering rate for the organic layers may differ from that of the metallic Eu ion such that sputtering may actually change the structure of the underlying layers. However, the Si, C and Eu XPS data from surface scans of samples with different bilayer thicknesses did provide some insights. We normalized each XPS atomic % signal to its value from one of the spot scans on the 2.5 bilayer sample and plot the change in relative signal intensity as a function of PEM thickness (figure 4).

The amount of detectable silicon from the quartz substrate steadily decreases with increasing PEM thickness. The fall-off in silicon signal intensity is consistent with the Si 2p approximate electron escape depth of 11.3–15.3 nm we

calculate from [18]. By contrast, the carbon signal, associated with the PEM, increases from the thinnest bilayers and reaches a steady state value when the PEM thickness is ~15 nm. Thus the variation of Si and C signals with bilayer thickness is qualitatively what is expected. The change in Eu XPS signal intensity is more difficult to interpret.

If all the Eu remained on the surface of the sample, we might expect the Eu XPS signal to scale similarly to the C XPS signal. As shown in figure 4, there are slight differences in the scaling, but given the variations in the Eu signals, it is hard to discern definitive trends. Nevertheless, figure 3 shows a clear increase in the Eu PL intensity for PEMs of 4.5 bilayer thickness, an increase that is not evidenced equally in the XPS spectra. A possible explanation might involve the diffusion of Eu from the surface through the PEM. Eu diffusing more deeply than the escape depth would not contribute to the Eu XPS signature measured at the surface. Other considerations involve different thickness-dependent inelastic scattering cross sections for the electrons.

Other studies have done a calibrated measurement of diffusion of small molecules into the PAH/PSS system over time. These studies suggest that molecules on the order of the size of Eu-DPA will in fact spread out from the surface towards the bottom of the film when the PEM is exposed to a solution of those molecules over minutes to hours [19]. These studies only used neutral molecules, so the diffusion mechanism and rate for negatively charged molecules such as Ln-DPA may differ. Furthermore, other studies of the structure of the PAH/PSS system suggest that when a PEM prepared at high pH is dipped into a low pH solution such as the Eu-DPA, previously uncharged clustered amine groups in the PAH become charged, leading to an opening up and swelling of the PEM [20]. Such an expansion with positively charged regions could allow a negatively charged molecule such as Eu-DPA, first attracted to the positive charge on the surface, to further diffuse through the PEM by attraction to positively charged regions below the surface. The Eu-DPA would then be embedded within the PEM upon drying of the sample.

While we have not done direct diffusion measurements on this system, our results are consistent with these studies. The change in PL intensity for different bilayer thicknesses and the XPS results imply that the Eu-DPA may diffuse to some degree below the surface of the PEM, but they do not show exactly where the Eu is distributed in the sample. The complexities of this diffusion process require further experiments and simulations to be properly understood.

We additionally note that the pH of the PAH solution decreases slightly as more layering steps are performed in a given run. This will affect the thickness and charge of each new PAH layer deposited, which may then affect the amount of Eu-DPA that can be incorporated. At this point, the variation in the luminescence intensity of the Eu^{3+} with PEM layer thickness, while not fully understood, offers the interesting possibility of modulating the incorporation of emitters into the multilayer structure. In the case of the Eu-DPA-PEM on the gold substrate, this result suggests the Eu-DPA is even closer to the gold substrate than originally thought. Therefore, the power of the DPA to protect the lanthanide from quenching and allow for strong emission even in very close proximity to the gold surface may be greater than previously thought.

We last consider that there may be additional ways to further control lanthanide emission intensity as a function of PEM thickness. As stated above, controlling the pH of the PAH solution will affect the thickness of the bilayer and available positive charge for binding the negatively charged Ln-DPA. The pH of the Ln-DPA solution will change how many amine groups become positively charged, thereby modifying how the PEM structure changes in solution and how much Ln-DPA will bind to it. Modifying the salt concentration of the PAH and PSS solutions will also change the structure of the PEM, influencing its ability to bind Ln-DPA.

4. Conclusion

We have demonstrated a straightforward process that allows charge-controlled binding of Ln-DPA light-emitting complexes into thin film PEMs. By integrating mixtures of different Ln-DPA molecules from solution, we have been able to tune the emission wavelength of these films. We have observed excellent emission intensity from the Ln-DPA-PEM films even when bound to metallic substrates. We have also observed that the emission intensity and linewidth remain robust over multiple months. In the future, we hope to use this method to embed these lanthanide emitters on patterned surfaces or on nanoparticles constructed from a variety of metallic and dielectric materials to further characterize their interaction with different substrates and nanostructures.

Acknowledgments

ASG acknowledges support from the National Science Foundation Graduate Research Fellowship Program under Grant No DGE–1144152. BLM acknowledges support from the STC Center for Integrated Quantum Materials under National Science Foundation Grant No DMR–1231319. This work was supported in part by the Defense Advanced Research Projects Agency QuASAR program Grant No W911NF-11-1-0228. This work was performed in part at the Harvard University Center for Nanoscale Systems (CNS), a member of the National Nanotechnology Coordinated Infrastructure Network (NNCI), which is supported by the National Science Foundation under NSF ECCS award No 1541959.

Author contributions

ASG performed and analyzed the experiments. BLM helped prepare Ln-DPA crystals, prepared Eu- and Tb-DPA mixed solutions, and bound Eu- and Tb-DPA mixtures to previously prepared PEMs. ASG and ELH discussed the results, co-wrote, and commented on the manuscript.

Conflict of interest

The authors declare no competing financial interest.

ORCID iDs

Andrew S Greenspon https://orcid.org/0000-0002-9631-7568

References

[1] Hennessy K, Badolato A, Winger M, Gerace D, Atat Uuml Re M, Gulde S, F Auml Lt S, Hu E L and Imamo Gbreve Lu A 2007 Quantum nature of a strongly coupled single quantum dot-cavity system *Nature* **445** 896

[2] Hussain R, Keene D, Noginova N and Durach M 2014 Spontaneous emission of electric and magnetic dipoles in the vicinity of thin and thick metal *Opt. Express* **22** 7744–55

[3] Bünzli J C G and Eliseeva S V 2010 Lanthanide NIR luminescence for telecommunications, bioanalyses and solar energy conversion *J. Rare Earths* **28** 824–42

[4] Wu J, Zhang H and Du S 2016 Tunable luminescence and white light emission of mixed lanthanide—organic frameworks based on polycarboxylate ligands *J. Mater. Chem.* C **4** 3364–74

[5] Bünzli J-C G 2009 Lanthanide luminescent bioprobes (LLBs) *Chem. Lett.* **38** 104–9

[6] Chen P and Holten-Andersen N 2015 Multistimuli-responsive white luminescent fluids using hybrid lanthanide metal-coordinate complex probes *Adv. Opt. Mater.* **3** 1041–6

[7] Chen P, Li Q, Grindy S and Holten-Andersen N 2015 White-light-emitting lanthanide metallogels with tunable luminescence and reversible stimuli-responsive properties *J. Am. Chem. Soc.* **137** 11590–3

[8] Andres J, Hersch R D, Moser J E and Chauvin A S 2014 A new anti-counterfeiting feature relying on invisible luminescent full color images printed with lanthanide-based inks *Adv. Funct. Mater.* **24** 5029–36

[9] Kumari A, Soni A K and Rai V K 2017 Near infrared to blue upconverting $Tm^{3+}/Yb^{3+}/Li^{+}$:$Gd_2(MoO_4)_3$ phosphors for light emitting display devices *Infrared Phys. Technol.* **81** 313–9

[10] Soni A K, Rai V K and Mahata M K 2017 Yb^{3+} sensitized $Na_2Y_2B_2O_7$:Er^{3+} phosphors in enhanced frequency upconversion, temperature sensing and field emission display *Mater. Res. Bull.* **89** 116–24

[11] Mukhopadhyay L and Rai V K 2017 Upconversion based near white light emission, intrinsic optical bistability and temperature sensing in $Er^{3+}/Tm^{3+}/Yb^{3+}/Li^{+}$:$NaZnPO_4$ phosphors *New J. Chem.* **41** 7650–61

[12] Liu H, Lu W, Wang H, Rao L, Yi Z, Zeng S and Hao J 2013 Simultaneous synthesis and amine-functionalization of single-phase $BaYF_5$:Yb/Er nanoprobe for dual-modal *in vivo* upconversion fluorescence and long-lasting x-ray computed tomography imaging *Nanoscale* **5** 6023

[13] Yi Z, Zeng S, Lu W, Wang H, Rao L, Liu H and Hao J 2014 Synergistic dual-modality *in vivo* upconversion luminescence/x-ray imaging and tracking of amine-functionalized $NaYbF_4$:Er nanoprobes *ACS Appl. Mater. Interfaces* **6** 3839–46

[14] Bunzli J G and Eliseeva S V 2010 Basics of lanthanide photophysics *Lanthanide Luminescence: Photophysical, Analytical and Biological Aspects* (*Springer Series Fluorescence*) (Berlin: Springer) pp 1–45

[15] Itano K, Choi J and Rubner M F 2005 Mechanism of the pH-Induced discontinuous swelling/deswelling transitions of poly (allylamine hydrochloride)-containing polyelectrolyte multilayer films *Macromolecules* **38** 3450–60

[16] Hiller J and Rubner M F 2003 Reversible molecular memory and pH-switchable swelling transitions in polyelectrolyte multilayers *Macromolecules* **36** 4078–83

[17] Anon 2008 Angle resolved XPS *Thermo-Scientific Application Note* 31014

[18] Cumpson P J 2001 Estimation of inelastic mean free paths for polymers and other organic materials: use of quantitative structure-property relationships *Surf. Interface Anal.* **31** 23–34

[19] von Klitzing R and Möhwald H 1996 A realistic diffusion model for ultrathin polyelectrolyte films *Macromolecules* **29** 6901–6

[20] Lichter J A and Rubner M F 2009 Polyelectrolyte multilayers with intrinsic antimicrobial functionality: the importance of mobile polycations *Langmuir* **25** 7686–94